atmosphere

MDPI

Article

A Theoretical Model for Predicting Visibility During Dust Events

Jin Li [1,2], Xiaoqian Ma [1,2], Yang Meng [3,*], Jun Lu [1,2] and Weiguang Tian [1,2]

[1] State Grid Economic and Technical Research Institute Co., Ltd., Beijing 102209, China; lijin@chinasperi.sgcc.com.cn (J.L.); mxqian228@163.com (X.M.); lujun@chinasperi.sgcc.com.com (J.L.); tianweiguang@chinasperi.sgcc.com.cn (W.T.)

[2] Icing and Safety of Power Facilities in the Transition Zone of Erlang Mountain Plateau Observation and Research Station of Sichuan Province, Ganzi 626100, China

[3] Key Laboratory of Mechanics on Disaster and Environment in Western China, The Ministry of Educational Department, Lanzhou University, Lanzhou 730315, China

* Correspondence: myang2024@lzu.edu.cn

Abstract

A physically based framework is developed to predict horizontal visibility during dust events by linking surface wind erosion, dust emission, near-surface dust concentration, and visibility. An analytical concentration–visibility relationship is derived using a heuristic closure condition. Dust concentration is further related to wind forcing through saltation-controlled dust emission and steady-state mass conservation, while a moment-balance entrainment model incorporates median particle size and soil cohesion into the threshold friction velocity. The concentration–visibility relationship is evaluated using observations from three published studies and captures the overall variation in the combined dataset with R^2 = 0.62. Under the same calibration conditions, the proposed relationship achieved the highest R^2 among all formulations examined, indicating that its functional form more effectively captures the nonlinear dependence of visibility on dust concentration in the combined dataset. By linking surface erodibility and aerodynamic forcing to atmospheric dust loading and visibility, the framework provides a physically based approach for dust-event visibility prediction. Further evaluation of the complete model chain requires synchronized observations of surface properties, particle entrainment, dust emission, concentration, and visibility.

Keywords: dust events; horizontal visibility; dust concentration; dust emission; threshold friction velocity; wind erosion

1. Introduction

Dust events are hazardous weather phenomena with widespread impacts in arid and semi-arid regions. Once large quantities of surface particles are entrained into the near-surface atmosphere, they can substantially increase particulate matter concentrations and the atmospheric extinction coefficient, leading to a rapid reduction in horizontal visibility and directly affecting road transportation, aviation operations, outdoor activities, and public health [1–5]. Compared with aerosol optical depth or particulate matter concentration, visibility provides a more direct measure of the practical impacts of dust events on transportation safety and human activities. Accurate prediction of dust-related visibility is therefore an important component of dust hazard classification, traffic risk management, and short-term warning systems. Previous observational studies have shown that dust events can reduce near-surface visibility to several kilometers or even a few hundred meters,

Check for updates

Academic Editor: Pavel Kishcha

Received: 11 August 2026
Revised: 28 August 2026
Accepted: 2 September 2026
Published: 16 September 2026

with visibility changes often evolving concurrently with particulate matter concentrations, aerosol chemical composition, and boundary-layer turbulence [6–8].

Under dusty conditions, visibility is primarily governed by the scattering and absorption of visible light by airborne particles, with variations controlled jointly by dust concentration, particle size distribution, particle shape, mineral composition, and complex refractive index [9,10]. Wind speed, boundary-layer height, and atmospheric stability regulate the emission, transport, and vertical mixing of dust particles, while relative humidity can alter atmospheric extinction through hygroscopic particle growth and the mixing of different aerosol types. Consequently, the same PM_{10} concentration may correspond to different visibility levels under different particle size distributions, source distances, and meteorological conditions. Early observational studies showed that the relationship between visibility and suspended dust concentration can generally be described by power-law, exponential, or approximately inverse relationships [11–15]. Subsequent studies conducted in Africa, East Asia, Mongolia, Australia, and the Middle East further demonstrated that the quantitative relationship between visibility and dust concentration is also influenced by seasonal variability, relative humidity, measurement methods, dust-event type, and the distance between the observation site and the dust source [16–24].

Empirical and statistical approaches have long been an important avenue of research on visibility during dust events. Some studies have used observed visibility to retrieve PM_{10} or total suspended particulate concentrations and, on this basis, to classify dust-event severity, reconstruct historical dust activity, or assess the intensity of dust events [17–25]. However, most of these studies have focused on estimating dust concentration from visibility, whereas comparatively less attention has been given to predicting future visibility from meteorological conditions and dust characteristics. Empirical relationships are generally dependent on specific regions, measurement instruments, and dust-event conditions, and their direct application to other regions can therefore introduce systematic biases. The quantitative relationship between visibility and PM_{10} established by Song et al. [18] for East Asia showed clear regional applicability; Baddock et al. [20] found significant differences in the visibility–dust concentration relationship between near-source and regional-transport conditions; and Mobarak Hassan and Alizadeh [23] reported that different functional forms may be appropriate for different visibility ranges. Consequently, a single fixed empirical relationship is unlikely to accurately represent visibility variations throughout the full evolution of a dust event, including its onset, intensification, transport, and decay.

With the development of numerical atmospheric models, researchers have increasingly estimated aerosol extinction coefficients from model-predicted dust emission, transport, deposition, particle size distributions, and near-surface particulate matter concentrations, and subsequently diagnosed horizontal visibility under dusty conditions. Early regional dust forecasting systems and models, including DREAM, GOCART, BSC-DREAM8b, and NMMB/BSC-Dust, laid the foundation for predicting dust concentration, particle size distributions, and aerosol optical properties [26–33]. However, model outputs are highly sensitive to surface erodibility, threshold conditions for particle entrainment, emission fluxes, particle size binning, boundary-layer parameterizations, and initial aerosol fields, and substantial differences remain among models in their simulations of dust concentrations and aerosol optical properties [33–37]. These uncertainties can propagate into calculations of the extinction coefficient and visibility, resulting in considerable uncertainty in the prediction of extremely low-visibility events. In recent years, machine learning and data assimilation approaches have also been applied directly to dust-visibility prediction. Xu et al. incorporated physical processes, including dust emission, vertical mixing, horizontal transport, and wet scavenging, as predictors in a machine-learning framework to forecast dust-visibility categories up to 72 h in advance. Their results showed that incorporating process-based information reduced prediction errors and suppressed nonphysical drift in the forecasts with increasing lead time [38]. Mei et al. assimilated high-density surface visibility observations into the WRF-Chem model, improving the initial aerosol field, extinction coefficient, and subsequent forecasts during dust events [39]. Despite these advances, the limited number of extremely low-visibility cases, imbalanced sample distributions among visibility categories, accumulation of numerical weather prediction errors, and limited cross-regional generalizability remain major constraints on the accuracy of dust-visibility prediction.

Overall, previous studies have established the effects of dust concentration, particle optical properties, and meteorological conditions on visibility and have developed several prediction approaches based on empirical statistics, numerical forecasting, and machine learning. However, these components have largely been investigated separately, and few models systematically link the physical processes of dust generation and transport with changes in near-surface particulate matter concentrations. This limitation is particularly important during severe dust events and extremely low-visibility conditions, where limited observational samples and complex nonlinear processes constrain both conventional empirical models and purely data-driven approaches. Therefore, this study develops a physically based framework for dust-visibility prediction. Through theoretical analysis, a quantitative relationship between visibility and dust concentration is derived from the physical processes governing dust emission, and meteorological forcing (wind speed) together with surface physical and mechanical properties, including particle size and soil cohesion, is incorporated into the mathematical formulation. The proposed framework may improve the physical basis for identifying and forecasting extremely low-visibility events and provide quantitative support for dust-hazard warning, road traffic management, and aviation operations.

2. Theoretical Model

2.1. The Mathematical Relationship Between Visibility and Dust Concentration

Previous observational studies have demonstrated a significant negative correlation between near-surface dust concentration and horizontal visibility under dusty conditions [11,15]. As the concentration of suspended dust particles in the atmosphere increases, enhanced scattering and absorption of visible light increase the atmospheric extinction coefficient, thereby reducing horizontal visibility. Based on this fundamental relationship, a heuristic model is developed here to quantitatively describe the relationship between dust concentration and visibility.

Let C denote the near-surface dust mass concentration and D_v the horizontal visibility under dusty conditions. The model is based on the following assumptions: for a given study region and dust event, the dominant optical properties, particle size distribution, and effects of humidity can be represented collectively by empirical parameters to be determined; within the applicable range of the model, dust concentration and visibility are related through a continuous, differentiable, and monotonic function; and the contributions of other aerosol components and background extinction are accounted for through a background concentration or empirical parameters. Accordingly, the model is intended to describe the mean concentration–visibility response under specific regional and observational conditions, and its parameters must be calibrated against measured data.

The dust concentration can be expressed as a function of visibility:

$$C = f(D_v) \tag{1}$$

Under the assumption of monotonicity, Equation (1) has an inverse function, allowing visibility to be expressed as a function of dust concentration:

$$D_v = g(C) = f^{-1}(C) \tag{2}$$

Substituting Equation (2) into Equation (1) yields the following identity:

$$C = f[g(C)] \tag{3}$$

Taking the first derivative of Equation (3) with respect to (C) gives:

$$1 = f'(D_v)\frac{dg(C)}{dC} \tag{4}$$

Further mathematical manipulation of Equation (4) yields:

$$0 = f''(D_v)\left[\frac{dg(C)}{dC}\right]^2 + f'(D_v)\frac{d^2g(C)}{dC^2} \tag{5}$$

Rearranging Equation (5) gives:

$$-\frac{f''(D_v)}{f'(D_v)} = \frac{d^2g(C)/dC^2}{[dg(C)/dC]^2} \tag{6}$$

Equation (6) is a mathematical identity satisfied by any twice-differentiable pair of inverse functions and therefore cannot, by itself, uniquely determine the specific forms of (f) or (g). To obtain an analytical expression with a small number of parameters that can be readily calibrated, the following closure assumption is introduced:

$$-\frac{f''(D_v)}{f'(D_v)} = \frac{d^2g(C)/dC^2}{[dg(C)/dC]^2} = \beta \tag{7}$$

where β is an effective optical-response parameter controlling the nonlinear sensitivity of visibility to dust concentration. Physically, the specific extinction coefficient determines the light extinction per unit dust mass and is influenced by particle size distribution and optical properties. Relative humidity can further modify particle size and scattering efficiency through hygroscopic growth, thereby affecting the fitted value of β. Thus, β integrates these optical and environmental effects and is condition-dependent.

Solving Equation (7) yields the following mathematical relationship between visibility and dust concentration:

$$D_v = D_r - \frac{1}{\beta}ln\left(\frac{C - C_b}{C_r}\right) \tag{8}$$

where D_r is the reference visibility and C_r is the reference dust concentration. The introduction of C_r ensures that the argument of the logarithmic function is dimensionless. C_b is an integration constant. These parameters can be determined by fitting the model to observational data.

2.2. Quantitative Analysis of Dust Concentrations

Atmospheric suspended dust originates primarily from soil wind erosion. When wind acts on an erodible surface, sand-sized particles are first transported by creep and saltation. The impact of saltating particles on the surface can disrupt soil aggregates and release finer particles that can enter suspension. Wind-tunnel experiments by Shao et al. showed that, under natural conditions, dust emission is primarily controlled by saltation bombardment, with the vertical dust emission flux being approximately proportional to the horizontal saltation flux [40]. Under certain conditions, the horizontal saltation flux increases approximately with the cube of friction velocity. For saltating particles of a given diameter (d_s) and emitted dust particles of diameter (d_i), the dust emission framework proposed by Shao et al. can be summarized as follows [41]:

$$F_d(d_i, d_s) = \alpha(d_i, d_s)Q(d_s) \tag{9}$$

where $F_d(d_i, d_s)$ is the dust emission flux of particles with diameter (d_i) generated by the impact of saltating particles with diameter (d_s); $Q(d_s)$is the horizontal saltation flux of particles with diameter (d_s); and $\alpha(d_i, d_s)$ is the dust emission efficiency. Integrating over all saltating particle sizes and emitted dust particle sizes yields the total vertical dust emission flux:

$$F_d = \int_{d_{imin}}^{dimax} \int_{d_{smin}}^{d_{smax}} \alpha(d_i,\ d_s)Q(d_s)dd_s dd_i \tag{10}$$

To obtain a reduced-parameter model, Equation (10) can be simplified as follows:

$$F_d = \overline{\alpha}Q \tag{11}$$

where $\overline{\alpha}$ is the integrated dust emission efficiency, which represents the combined effects of factors such as soil particle size distribution, aggregate state, surface crusting, and soil strength. The horizontal saltation flux is commonly expressed as [42]:

$$Q = C_Q \frac{\rho_a}{g} u_*^3 \left[1 - \left(\frac{u_{*t}}{u_*}\right)^2\right] \tag{12}$$

where C_Q is a calibration coefficient, ρ_a is the air density, and u_* and u_{*t} denote the surface friction velocity and the threshold friction velocity for particle entrainment, respectively.

Equations (11) and (12) can be combined to quantitatively estimate dust concentration. Because dust emission from wind erosion is a major source of atmospheric suspended particulate matter, this study focuses on establishing a mathematical relationship between dust concentration and dust emission flux. Under wind forcing, dust particles move stochastically in three dimensions. Under steady-state conditions, the conservation equation for dust mass in the horizontal direction can be written as:

$$U\frac{dC}{dx} = F_d - v_e C \tag{13}$$

where U is the mean streamwise wind speed, and v_e is the effective removal velocity, which collectively represents mass losses caused by gravitational settling, surface deposition, and turbulent diffusion. Integrating Equation (13) yields the following expression:

$$C(x) = c_0 \exp\left(-\frac{v_e x}{U}\right) + \frac{F_d}{v_e}\left[1 - \exp\left(-\frac{v_e x}{U}\right)\right] \tag{14}$$

where c_0 is a reference concentration that can be determined by fitting the model to observational data. Equation (14) provides an analytical relationship between the streamwise distribution of dust concentration and the dust emission flux under steady-state conditions, with wind speed playing an important role. Based on Equation (14), the dust concentration can be estimated at any location. Assuming that dust concentration is observed at x_n, the concentration C at the observation point can be expressed as:

$$C(x) = c_0 \exp\left(-\frac{v_e x_n}{U}\right) + \frac{F_d}{v_e}\left[1 - \exp\left(-\frac{v_e x_n}{U}\right)\right] = c_0 \exp\left(-\frac{v'_e}{U}\right) + \frac{F_d}{v_e}\left[1 - \exp\left(-\frac{v'_e}{U}\right)\right] \tag{15}$$

where v_e' represents the integrated removal velocity along the transport path and, for simplicity, is treated as an empirical coefficient.

Analysis of Equation (15) shows that application of the above formulation still requires an appropriate estimate of the threshold friction velocity for particle entrainment. Although Shao and Lu (2000) derived an analytical expression for the threshold friction velocity of dry sand particles, their formulation primarily addresses the specific case of dry, loose particles and therefore cannot provide a unified description of erosion thresholds across different surface conditions [43]. To address this limitation, we adopt the moment-balance-based parameterization developed by Meng et al. (2026) to reformulate the threshold for particle entrainment [44]. This parameterization has been evaluated against wind-tunnel measurements of crust mechanical properties and wind erosion responses, providing experimental support for its application to wind-driven particle entrainment. The arrangement of surface particles is simplified as a three-sphere configuration, as Figure 1 illustrated below:

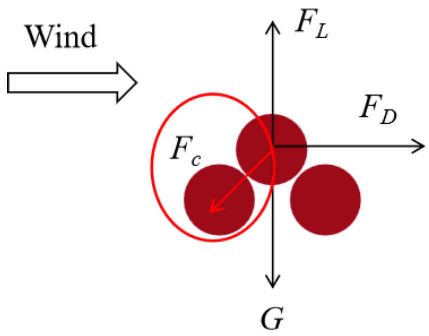

Figure 1. A schematic diagram of the force analysis for soil particle entrainment.

A surface particle subjected to airflow is primarily acted upon by the drag force (F_D), lift force (F_L), effective gravitational force (G), and interparticle bonding force (F_c). These forces can be expressed mathematically as follows:

$$F_D = \frac{1}{2} C_D \rho_a A_D u_*^2 = K_D \rho_a d^2 u_*^2 \tag{16}$$

$$F_L = \frac{1}{2} C_L \rho_a A_L u_*^2 = K_L \rho_a d^2 u_*^2 \tag{17}$$

$$G = (\rho_s - \rho_a) g V_s = K_g (\rho_s - \rho_a) g d^3 \tag{18}$$

$$F_c = c A_c = K_c c d^2 \tag{19}$$

where C_D and C_L are the drag and lift coefficients, respectively; A_D, A_L and A_c denote the frontal area, lift-force area, and interparticle contact area, respectively. K_D and K_L are integrated coefficients accounting for the coupled effects of near-bed turbulence and particle shape, whereas K_g and K_c are particle-shape correction coefficients. d is the median particle diameter of the soil surface, and c is the soil cohesion, which can be determined from shear-strength tests.

Shao and Lu (2000) assumed that the interparticle bonding force is proportional to the median soil particle diameter [43]. Although this relationship is applicable to dry sandy soils, its applicability to other soil types remains uncertain. In contrast, Equation (20) incorporates readily measurable soil mechanical properties into the quantitative representation of cohesion, giving the model a clearer physical basis and potentially broader applicability to different soil surfaces.

The threshold condition for particle entrainment is determined using the moment-balance criterion, which can be expressed mathematically as follows:

$$F_D L_D + F_L L_L = G L_G + F_c L_c \tag{20}$$

where L_D, L_L, L_G, L_c denote the moment arms of the drag force, lift force, effective gravitational force, and interparticle bonding force, respectively. These moment arms are assumed to be proportional to the median particle diameter d, such that:

$$L_D = a_D d, \;\; L_L = a_L d, \;\; L_G = a_G d, \;\; L_c = a_c d \tag{21}$$

where a_D, a_L, a_G, a_c are proportionality coefficients. Combining Equations (16)–(21), the threshold friction velocity for particle entrainment can be expressed as:

$$u_{*t} = A\sqrt{\frac{\rho_s - \rho_a}{\rho_a} g d + B\frac{c}{\rho_a}} \tag{22}$$

where A and B are empirical coefficients.

Combining Equations (8), (15), and (22) yields an integrated mathematical relationship linking visibility to wind speed and soil properties. This framework provides a potentially useful computational tool for dust-event forecasting and warning.

3. Model Validation

We developed an integrated physical framework that explicitly accounts for the relationship between atmospheric dust concentration and dust emission and further links these processes to visibility. Our literature review indicates that studies simultaneously measuring surface properties, dust emission, atmospheric dust concentration, and visibility are extremely scarce, making it difficult to obtain observational data suitable for directly evaluating the linkage between dust emission and visibility. Fortunately, paired observations of atmospheric dust concentration and visibility are available from several published studies. Given this limitation, we evaluate the concentration–visibility component of the proposed framework by directly testing the mathematical relationship between atmospheric dust concentration and visibility, namely Equation (8).

The particle-entrainment component of the framework is supported by previous theoretical and observational evidence. The entrainment formulation adopted here follows the moment-balance parameterization of Meng et al. (2026), whose effectiveness in representing wind-driven particle entrainment was evaluated against wind-tunnel observations [44]. Independent field observations also support the physical controls represented in Equation (22). Jugder et al. (2014) reported clear differences in threshold wind speed among several Gobi Desert sites and attributed these differences to variations in soil texture and surface aggregation, indicating that particle initiation depends not only on aerodynamic forcing but also on surface particle properties [22]. This is consistent with Equation (22), in which particle size and interparticle cohesion jointly determine the entrainment threshold. Shao et al. (2003) incorporated threshold friction velocity as the first step of an integrated wind-erosion scheme, followed by saltation transport and dust emission, and evaluated the resulting near-surface dust concentrations against observations across Northeast Asia [45]. This provides additional evidence that an appropriately parameterized entrainment threshold is a physically meaningful control on subsequent dust emission and atmospheric loading. In contrast, the observations of Mobarak Hassan and Alizadeh (2022) [23] mainly reflect the concentration–visibility response under conditions affected by both local and transported dust and therefore provide limited direct constraint on surface particle initiation. Taken together, these studies support the physical basis and effectiveness of the particle-entrainment component, while the present dataset is used primarily for direct evaluation of the concentration–visibility relationship.

The accuracy of Equation (8) can provide indirect support for the plausibility of the proposed theoretical framework. Conceptually, the framework consists of two main components: the relationship between dust concentration and visibility, and the relationship between dust emission flux and atmospheric dust concentration. A significant relationship between dust emission and atmospheric dust concentration has already been established in previous aeolian-physics studies [40–42]. Therefore, if the mathematical relationship between dust concentration and visibility can be reproduced with sufficient accuracy, this would provide strong support for the overall consistency of the proposed framework. The observational data used to evaluate Equation (8) were obtained from Shao et al. (2003) [45], Jugder et al. (2014) [22], and Mobarak Hassan and Alizadeh (2022) [23]. A comparison between the predictions of Equation (8) and the observational data is presented in Figure 2.

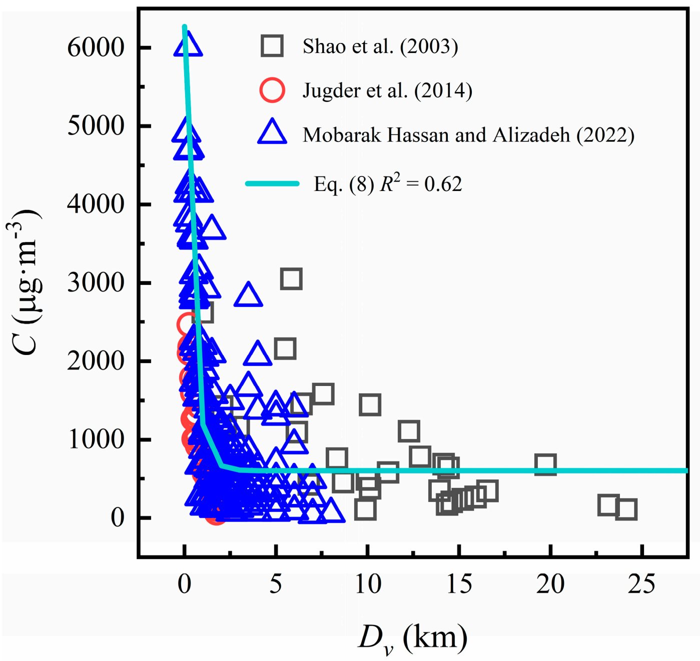

Figure 2. Comparison between the values predicted by Equation (8) and the observed values [22,23,45].

Fitting Equation (8) to the observational data yields the following relationship between visibility and dust concentration:

$$C = 602.885 + \exp[2.235 \times (3.867 - D_v)] \tag{23}$$

As shown in Figure 2, Equation (8) agrees reasonably well with the observational data, with (R^2 = 0.62), indicating that it captures the overall variation in visibility with dust concentration. Further evaluation showed a visibility RMSE of 3.32 km within the applicable range of the calibrated relationship. The RMSE decreased to 0.99, 0.60, and 0.44 km for $D_v \leq 5$, 3, and 2 km, respectively, indicating better accuracy under severe low-visibility conditions relevant to dust-event warning. Moreover, the overall model structure is developed around Equation (8), which serves as a key link between surface wind-erosion processes and atmospheric visibility prediction. By incorporating the physical processes governing dust emission from wind-eroded surfaces, the framework provides a physically based representation of visibility variations and addresses some of the limitations of conventional empirical approaches. The agreement between Equation (8) and the observational data therefore provides indirect support for the physical plausibility of the overall theoretical framework.

4. Discussion

4.1. Comparison with Previous Models

Accurate prediction of visibility during dust events is an important scientific issue in aeolian research. To date, a number of mathematical formulations have been developed to quantitatively describe the relationship between dust conditions and visibility. Based on a systematic review of the literature, several representative and widely used prediction equations are summarized in Table 1.

Table 1. Summary of Classical Formulations Relating Dust Concentration to Visibility.

References	Equations	Visibility Range	Study Area
D'Almeida, 1986 [15]	$C = 914.06 \times D_v^{-0.73} + 19.03$	200 m–40 km	Nigeria
Chung et al., 2003 [46]	$C = 1120 \times \exp(-0.2733 \times D_v)$		Korea and China
Shao et al., 2003 [45]	$C = \begin{cases} 3802.29 \times D_v^{-0.84} & D_v < 3.5\text{km} \\ \exp(-0.11 \times D_v + 7.62) & D_v \geq 3.5\text{km} \end{cases}$		Northeast Asia
Dayan et al., 2008 [47]	$C = -505\ln(D_v) + 2264$	1–5 km	Hazerim, Israel
Camino et al., 2015 [21]	$C = 1772.24 \times D_v^{-1.1} + 19.03$	4–75 km	North Africa

The values predicted using the equations listed in Table 1 were compared with the corresponding observations, and the coefficient of determination (R^2) was calculated, as shown in Figures 3–7. For consistency, the comparison was performed in terms of dust concentration; that is, dust concentration was estimated from the observed visibility using each equation and then compared with the measured dust concentration.

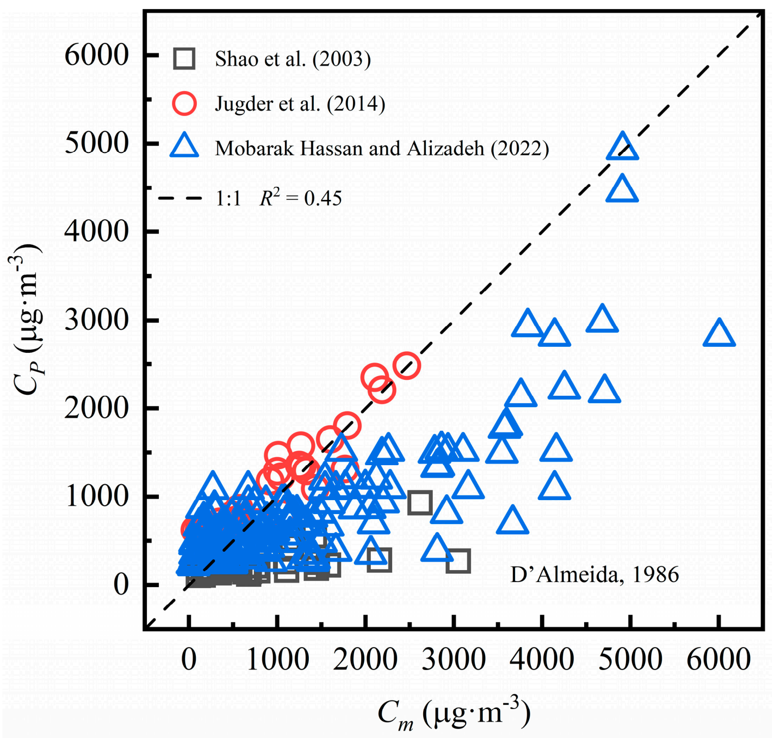

Figure 3. Comparison between the values predicted by the D'Almeida model and the observed values [15,22,23,45].

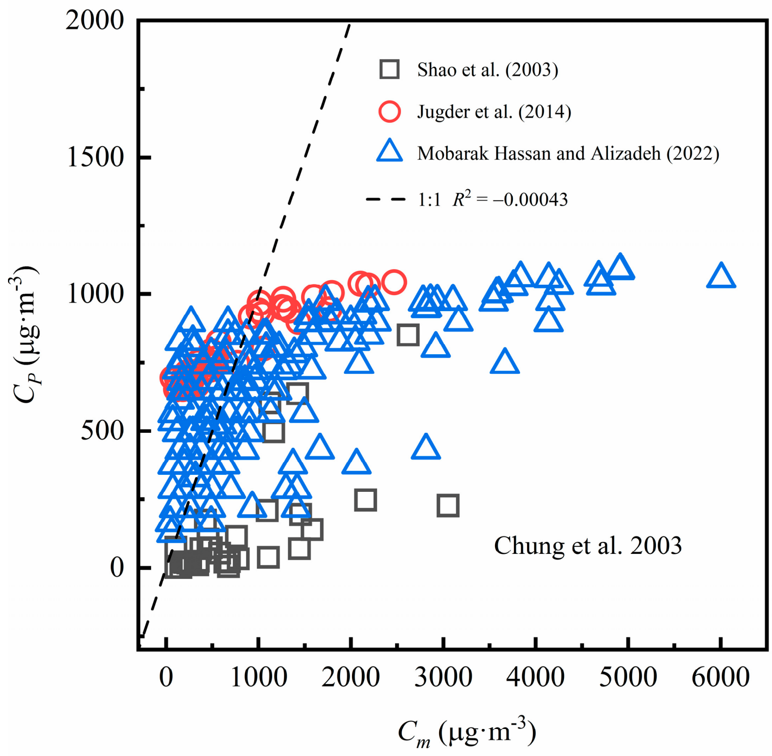

Figure 4. Comparison between the values predicted by the Chung et al. model and the observed values [22,23,45,46].

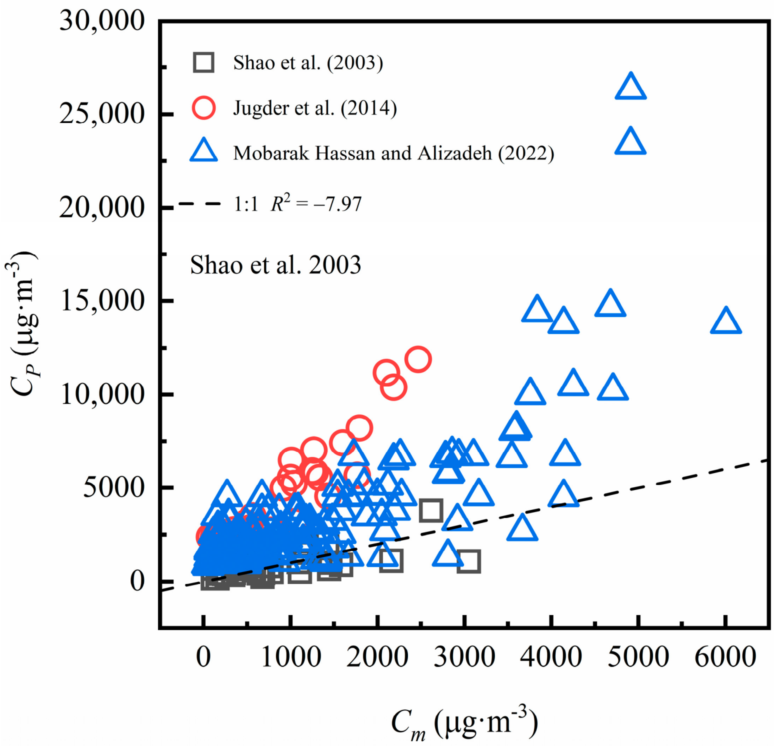

Figure 5. Comparison between the values predicted by the Shao et al. model and the observed values [22,23,45].

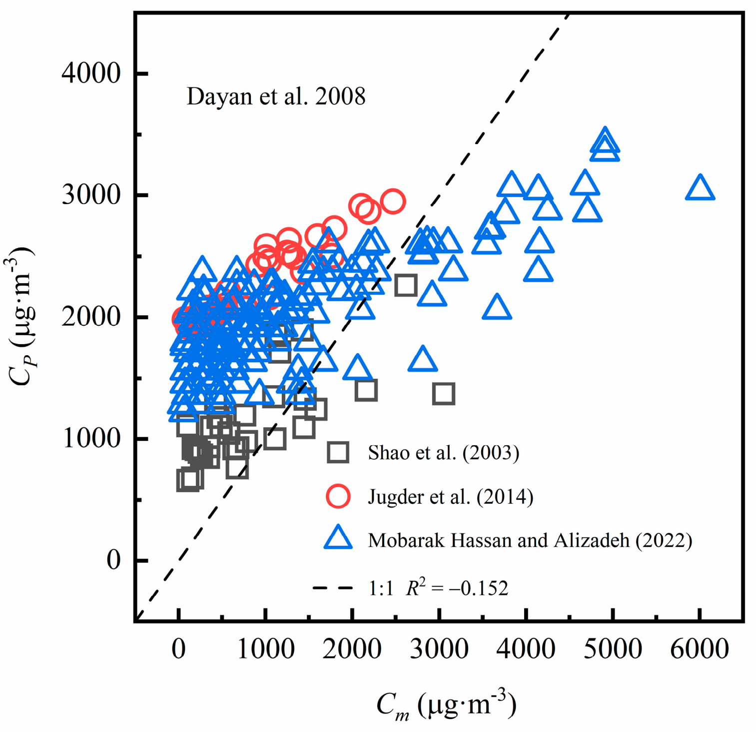

Figure 6. Comparison between the values predicted by the Dayan et al. model and the observed values [22,23,45,47].

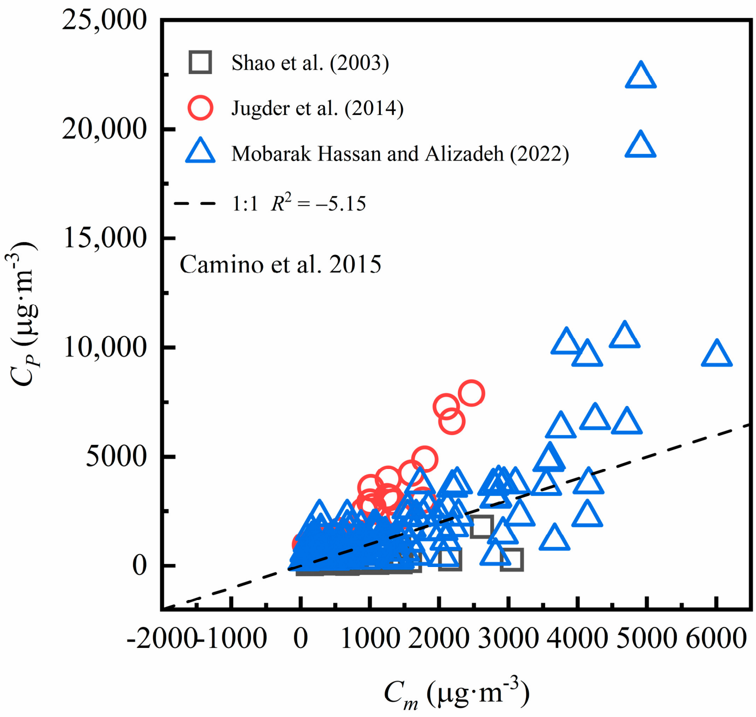

Figure 7. Comparison between the values predicted by the Camino et al. model and the observed values [21–23,45].

As shown in Figures 3–7, the predictive performance of the empirical models varies substantially when applied to the combined dataset. The D'Almeida model achieves an (R^2) of 0.45, representing the best performance among the five existing models considered, although the predicted values still show considerable scatter. The (R^2) values for the Chung et al., Shao et al., Dayan et al., and Camino et al. models are −0.00043, −7.97, −0.152, and

−5.15, respectively. Negative (R^2) values indicate that, for the present combined dataset, the prediction errors of these models exceed those obtained by simply using the mean of the observations as a constant predictor. Figures 3–7 also show that the models exhibit varying degrees of overestimation or underestimation, with these biases becoming more pronounced at higher dust concentrations. In comparison, the theoretical model developed in this study achieves an (R^2) of 0.62 for the same observational dataset and more effectively captures the overall variation in dust concentration with visibility.

It should be emphasized that the comparison in Figures 3–7 was based on the coefficients reported in the original studies, whereas Equation (8) was calibrated using the present combined dataset. Therefore, the differences among these models reflect both their mathematical forms and the regional dependence of their original parameterizations, and the comparison does not provide a fully equivalent assessment of predictive performance. The poor performance of several classical formulations suggests that direct transfer of published coefficients across regions may introduce substantial bias. To further evaluate the effect of model form under consistent calibration conditions, the coefficients of the classical formulations were recalibrated using the same combined dataset, as described in Section 4.2.

4.2. Recalibration and Comparison of Classical Visibility Models

To provide a consistent calibration basis, the adjustable coefficients of the classical models listed in Table 1 were recalibrated using the same combined observational dataset employed for Equation (8), while their original functional forms were retained. The D'Almeida (1986) [15] and Camino et al. (2015) [21] models have the same mathematical form; consequently, recalibration produced the same optimal coefficients and identical predictions, and their results are presented together in Figure 8.

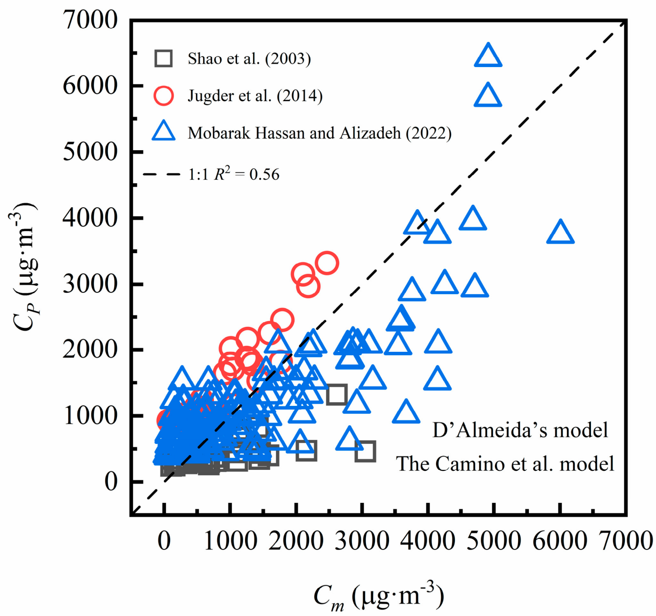

Figure 8. Comparison between the values predicted by the recalibrated D'Almeida/Camino model and the observed values [22,23,45].

Recalibration substantially improved the agreement between predicted and measured dust concentrations. The recalibrated D'Almeida/Camino model achieved an (R^2) of 0.56 (Figure 8), while the Chung et al., Shao et al., and Dayan et al. models yielded (R^2) values of 0.50, 0.59, and 0.38, respectively (Figures 9–11). Compared with the results obtained using the originally published coefficients, the performance of all classical formulations improved after recalibration. The particularly large improvement of several models indicates that their poor performance in Section 4.1 was strongly influenced by the transfer of region-specific coefficients to the present combined dataset.

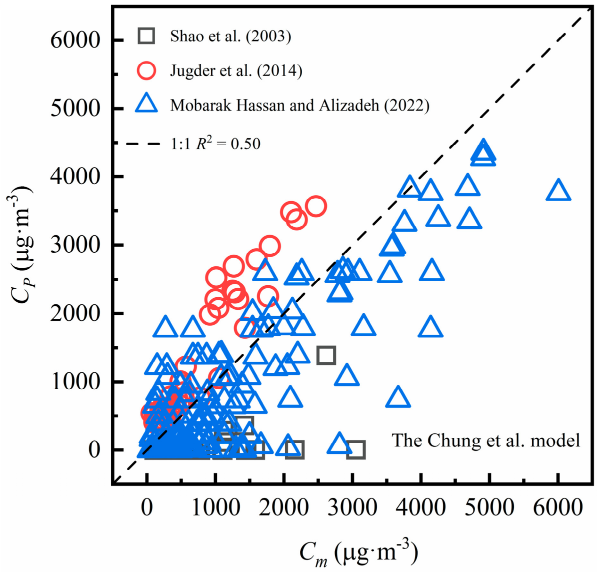

Figure 9. Comparison between the values predicted by the recalibrated Chung et al. model and the observed values [22,23,45].

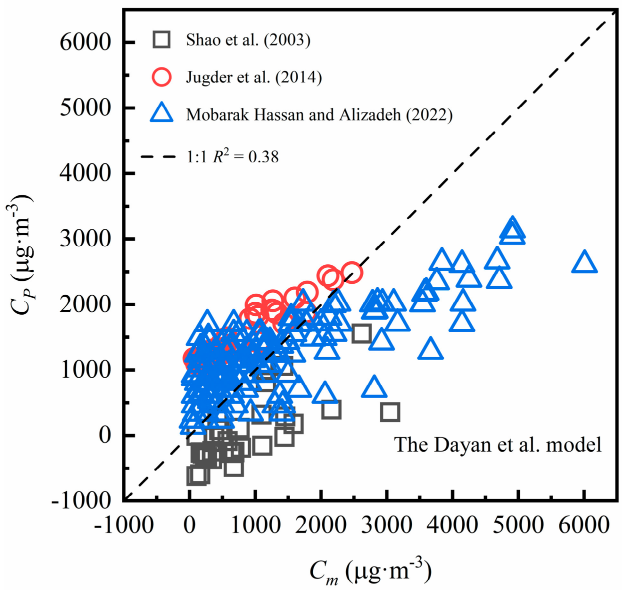

Figure 10. Comparison between the values predicted by the recalibrated Dayan et al. model and the observed values [22,23,45].

Among the recalibrated classical formulations, the Shao et al. model showed the highest agreement with the observations (R^2 = 0.59), followed by the D'Almeida/Camino (R^2 = 0.56) and Chung et al. (R^2 = 0.50) models. The Dayan et al. model showed the lowest agreement (R^2 = 0.38) and exhibited relatively large deviations at higher dust concentrations. Under the same calibration conditions, Equation (8) achieved the highest (R^2) of 0.62, demonstrating the best overall agreement with the combined observations among all formulations considered. This result indicates that the proposed functional form captures the nonlinear relationship between dust concentration and visibility more effectively than the recalibrated classical models. The comparison also shows that both parameter regionality and model structure contribute to differences in model performance across datasets.

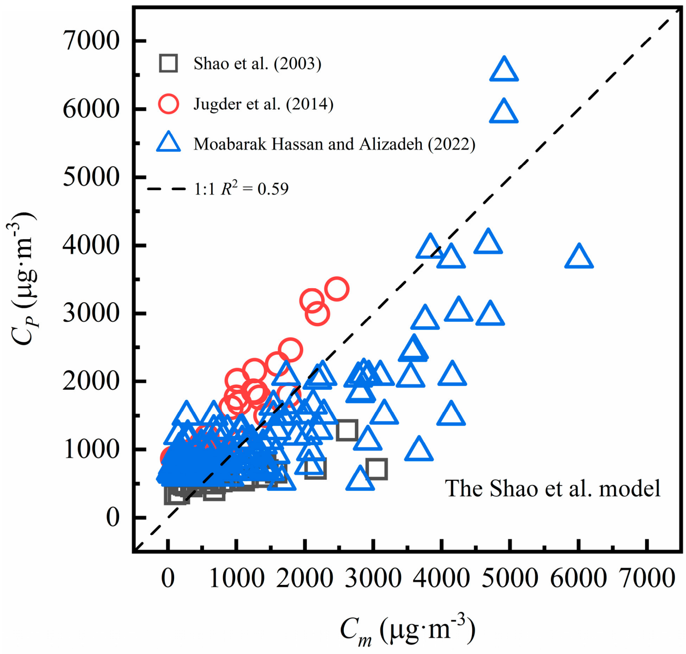

Figure 11. Comparison between the values predicted by the recalibrated Shao et al. model and the observed values [22,23,45].

4.3. Physical Meaning, Applicability, and Limitations of the Model

The main distinction between the present model and conventional empirical relationships between dust concentration and visibility is that the proposed framework extends visibility prediction to the physical processes of surface wind erosion and dust emission. The model first describes dust production using the horizontal saltation flux and dust emission efficiency, and then estimates near-surface dust concentration through mass conservation. A moment-balance criterion for particle entrainment is subsequently introduced to incorporate surface particle size and soil cohesion into the threshold friction velocity. In this way, a mathematical linkage is established among wind speed, surface properties, dust emission, dust concentration, and visibility.

This formulation allows the resistance of the land surface to wind erosion to regulate dust emission through the threshold for particle entrainment, which in turn affects near-surface dust concentration and visibility. The model can therefore explain why similar airflow conditions may produce different visibility reductions over surfaces with different erodibility. By incorporating surface physical and mechanical properties, particularly particle size and soil cohesion, the framework can also represent spatial variations in dust emission. The regional dependence of the model mainly arises from its parameterization rather than from the underlying physical framework. The relationships governing particle entrainment, moment balance, saltation transport, and dust emission are generally applicable, whereas regional differences are represented by parameters describing local surface and atmospheric conditions. In particular, the empirical coefficients (A) and (B) characterize the threshold friction velocity, while (β) reflects regional differences in the concentration–visibility response associated with aerosol properties and relative humidity. Other calibrated parameters related to dust emission and transport may likewise vary among regions. Thus, application to a new region mainly requires recalibration of the relevant parameters while retaining the same physical framework. Compared with approaches that estimate particulate matter concentration solely from visibility, the proposed model retains key controls on dust generation and provides a basis for integrating surface wind-erosion properties with meteorological variables.

It should be noted that the current model is still based on several simplifying assumptions. First, the dust transport equation assumes steady-state conditions, while processes such as gravitational settling, surface deposition, and turbulent diffusion are collectively represented by an effective removal velocity. Consequently, the model cannot fully describe the transient evolution of dust events during their onset, development, and decay. Second, the effects of particle size distribution, particle optical properties, relative humidity, and background aerosols on visibility are incorporated collectively into empirical parameters. Although this simplification reduces the number of required parameters, it also introduces a degree of regional dependence. More importantly, the available observational data allow only the dust concentration–visibility relationship described by Equation (8) to be directly evaluated. Because simultaneous observations of surface physical and mechanical properties, friction velocity, dust emission flux, near-surface dust concentration, and visibility remain very limited, the complete computational chain from surface particle entrainment to the resulting visibility response has not yet been independently validated.

Future studies should combine synchronized wind-tunnel or field measurements of surface properties, friction velocity, sand transport, dust emission, particulate concentration, and visibility to evaluate the model components and associated parameters. Transient transport, particle-size effects, relative humidity, and boundary-layer structure should also be incorporated to better define model applicability. In parallel, the framework can be further nondimensionalized using characteristic scales such as (C_r), (D_r), and (u_{*t}), leading to variables including (C/C_r), (D_v/D_r), and (U/u_{*t}). Such a formulation may reduce apparent regional dependence, facilitate comparison among different environments, and improve parameter transferability, although some parameters related to aerosol properties, humidity, and dust-emission efficiency may remain region-dependent.

5. Conclusions

This study develops a physically based framework for predicting horizontal visibility during dust events by linking surface wind erosion, dust emission, near-surface dust concentration, and visibility. The framework combines saltation-controlled dust emission, steady-state dust transport, and a moment-balance particle-entrainment formulation. By incorporating wind speed, median particle size, and soil cohesion into the threshold friction velocity, the model allows variations in surface erodibility to be propagated through dust emission and concentration to the resulting visibility response.

The concentration–visibility relationship was evaluated using observations from three published studies and reproduced the overall variation in the combined dataset with R^2 = 0.62. Under the same calibration conditions, the proposed relationship achieved the highest R^2 among the formulations examined, indicating that its functional form provides a more effective representation of the nonlinear concentration–visibility relationship for the present dataset. The framework therefore provides a simplified physical basis for visibility prediction that retains the effects of both aerodynamic forcing and surface properties. Further evaluation of the complete model chain requires synchronized measurements of surface properties, particle entrainment, dust emission, dust concentration, and visibility.

Author Contributions: Conceptualization, J.L. (Jin Li); methodology, X.M.; software, J.L. (Jin Li); validation, X.M.; formal analysis, Y.M.; investigation, X.M.; writing—original draft preparation, J.L. (Jin Li); writing—review and editing, W.T.; visualization, W.T. and Y.M.; supervision, J.L. (Jun Lu) and W.T.; funding acquisition, J.L. (Jun Lu). All authors have read and agreed to the published version of the manuscript.

Funding: This research was funded by the State Grid Science and Technology Project "Research on the spatial distribution of wind and sand and their impact on the total electric field in desert area of the western China" (Grant No. 5200-202356805A-3-8-KJ).

Data Availability Statement: The original contributions presented in this study are included in the article. Further inquiries can be directed to the corresponding author.

Conflicts of Interest: Co-author Jin Li is from State Grid Economic and Technical Research Institute Co., Ltd., and there are no conflicts of interest among the other authors.

References

1. Middleton, N. Desert dust hazards: A global review. *Aeolian Res.* **2017**, *24*, 53–63. [CrossRef]
2. Goudie, A. Desert dust and human health disorders. *Environ. Int.* **2014**, *63*, 101–113. [CrossRef] [PubMed]
3. Prospero, J.; Ginoux, P.; Torres, O.; Nicholson, S.; Gill, T. Environmental characterization of global sources of atmospheric soil dust identified with the Nimbus 7 Total Ozone Mapping Spectrometer (TOMS) absorbing aerosol product. *Rev. Geophys.* **2002**, *40*, 2-1–2-31. [CrossRef]
4. Shao, Y.; Wyrwoll, K.; Chappell, A.; Huang, J.; Lin, Z.; McTainsh, G.; Mikami, M.; Tanaka, T.; Wang, X.; Yoon, S. Dust cycle: An emerging core theme in Earth system science. *Aeolian Res.* **2011**, *2*, 181–204. [CrossRef]
5. Kok, J.; Storelvmo, T.; Karydis, V.A.; Adebiyi, A.A.; Mahowald, N.M.; Evan, A.T.; He, C.; Leung, D.M. Mineral dust aerosol impacts on global climate and climate change. *Nat. Rev. Earth Environ.* **2023**, *4*, 71–86. [CrossRef]
6. Fu, P.; Zhong, S.; Huang, J.; Song, G. An observational study of aerosol and turbulence properties during dust storms in northwest China. *J. Geophys. Res. Atmos.* **2012**, *117*, D09202. [CrossRef]
7. Cao, C.; Zheng, S.; Singh, R.P. Characteristics of aerosol optical properties and meteorological parameters during three major dust events (2005–2010) over Beijing, China. *Atmos. Res.* **2014**, *150*, 129–142. [CrossRef]
8. Cabello, M.; Orza, J.A.G.; Barrero, M.A.; Gordo, E.; Berasaluce, A.; Cantón, L.; Dueñas, C.; Fernández, M.C.; Pérez, M. Spatial and temporal variation of the impact of an extreme Saharan dust event. *J. Geophys. Res. Atmos.* **2012**, *117*, D11204. [CrossRef]
9. Malm, W.C.; Hand, J.L. An examination of the physical and optical properties of aerosols collected in the IMPROVE programme. *Atmos. Environ.* **2007**, *41*, 3407–3427. [CrossRef]
10. Dubovik, O.; Holben, B.; Eck, T.F.; Smirnov, A.; Kaufman, Y.J.; King, M.D.; Tanre, D.; Slutsker, I. Variability of absorption and optical properties of key aerosol types observed in worldwide locations. *J. Atmos. Sci.* **2002**, *59*, 590–608. [CrossRef]
11. Chepil, W.S.; Woodruff, N.P. Sedimentary characteristics of dust storms, Part II: Visibility and dust concentration. *Am. J. Sci.* **1957**, *255*, 104–114. [CrossRef]
12. Patterson, E.M.; Gillette, D.A. Measurements of visibility versus mass concentration for airborne soil particles. *Atmos. Environ.* **1977**, *11*, 193–196. [CrossRef]
13. Patterson, E.M. Atmospheric extinction between 0.55 µm and 10.6 µm due to soil-derived aerosols. *Appl. Opt.* **1977**, *16*, 2414–2418. [CrossRef] [PubMed]
14. Cachorro, V.E.; Tanré, D. The correlation between particle mass loading and extinction: Application to desert dust aerosol content estimation. *Remote Sens. Environ.* **1997**, *60*, 187–194. [CrossRef]
15. D'Almeida, G.A. A model for Saharan dust transport. *J. Clim. Appl. Meteorol.* **1986**, *25*, 903–916. [CrossRef]
16. N'Tchayi Mbourou, G.; Bertrand, J.J.; Nicholson, S.E. The diurnal and seasonal cycles of wind-borne dust over Africa north of the equator. *J. Clim. Appl. Meteorol.* **1997**, *36*, 868–882. [CrossRef]
17. Mahowald, N.M.; Ballantine, J.A.; Feddema, J.; Ramankutty, N. Global trends in visibility: Implications for dust sources. *Atmos. Chem. Phys.* **2007**, *7*, 3309–3339. [CrossRef]
18. Song, Z.; Wang, J.; Wang, S. Quantitative classification of northeast Asian dust events. *J. Geophys. Res. Atmos.* **2007**, *112*, D04211. [CrossRef]
19. Wang, Y.; Zhang, X.; Gong, S.; Zhou, C.; Hu, X.; Liu, H.; Niu, T.; Yang, Y. Surface observation of sand and dust storm in East Asia and its application in CUACE/Dust. *Atmos. Chem. Phys.* **2008**, *8*, 545–553. [CrossRef]
20. Baddock, M.C.; Strong, C.L.; Leys, J.F.; Heidenreich, S.K.; Tews, E.K.; McTainsh, G.H. A visibility and total suspended dust relationship. *Atmos. Environ.* **2014**, *89*, 329–336. [CrossRef]
21. Camino, C.; Cuevas, E.; Basart, S.; Alonso-Pérez, S.; Baldasano, J.M.; Terradellas, E.; Marticorena, B.; Rodríguez, S.; Berjón, A. An empirical equation to estimate mineral dust concentrations from visibility observations in Northern Africa. *Aeolian Res.* **2015**, *16*, 55–68. [CrossRef]
22. Jugder, D.; Shinoda, M.; Kimura, R.; Batbold, A.; Amarjargal, D. Quantitative analysis of windblown dust concentrations of PM_{10} and $PM_{2.5}$ during dust events in Mongolia. *Aeolian Res.* **2014**, *14*, 3–13. [CrossRef]
23. Mobarak Hassan, E.; Alizadeh, O. Dust events in southwestern Iran: Estimation of PM_{10} concentration based on horizontal visibility during dust events. *Int. J. Climatol.* **2022**, *42*, 5159–5172. [CrossRef]

24. Maleki, H.; Sorooshian, A.; Alam, K. The impact of meteorological parameters on PM_{10} and visibility during the Middle Eastern dust storms. *J. Environ. Health Sci. Eng.* **2022**, *20*, 495–507. [CrossRef] [PubMed]
25. Xi, X. Revisiting the recent dust trends and climate drivers using horizontal visibility and present-weather observations. *J. Geophys. Res. Atmos.* **2021**, *126*, e2021JD034687. [CrossRef]
26. Chin, M.; Ginoux, P.; Kinne, S.; Torres, O.; Holben, B.N.; Duncan, B.N.; Martin, R.V.; Logan, J.A.; Higurashi, A.; Nakajima, T. Tropospheric aerosol optical thickness from the GOCART model and comparisons with satellite and Sun photometer measurements. *J. Atmos. Sci.* **2002**, *59*, 461–483. [CrossRef]
27. Shao, Y.; Leslie, L.M.; Wang, J. Numerical simulation of the October 2002 dust event in Australia. *J. Geophys. Res. Atmos.* **2007**, *112*, D08207. [CrossRef]
28. Nickovic, S.; Kallos, G.; Papadopoulos, A.; Kakaliagou, O. A model for prediction of desert dust cycle in the atmosphere. *J. Geophys. Res. Atmos.* **2001**, *106*, 18113–18129. [CrossRef]
29. Ginoux, P.; Chin, M.; Tegen, I.; Prospeo, J.M.; Holbe, B. Sources and distributions of dust aerosols simulated with the GOCART model. *J. Geophys. Res. Atmos.* **2001**, *106*, 20255–20273. [CrossRef]
30. Pérez, C.; Haustein, K.; Janjic, Z.; Jorba, O.; Huneeus, N.; Baldasano, J.M.; Black, T.; Basart, S.; Nickovic, S.; Miller, R.L.; et al. Atmospheric dust modeling from meso to global scales with the online NMMB/BSC-Dust model, Part 1, Model description, annual simulations and evaluation. *Atmos. Chem. Phys.* **2011**, *11*, 13001–13027. [CrossRef]
31. Hong, S.K.; Ryoo, S.-B.; Kim, J.; Lee, S.-S. Prediction of Asian dust days over northern China using the KMA-ADAM2 model. *Weather Forecast.* **2019**, *34*, 1777–1787. [CrossRef]
32. Yin, D.; Nickovic, S.; Barbaris, B.; Chandy, B.; Sprigg, W.A. Modeling wind-blown desert dust in the southwestern United States for public health warning: A case study. *Atmos. Environ.* **2005**, *39*, 6243–6254. [CrossRef]
33. Huneeus, N.; Schulz, M.; Balkanski, Y.; Griesfeller, J.; Prospero, J.; Kinne, S.; Bauer, S.; Boucher, O.; Chin, M.; Dentener, F.; et al. Global dust model intercomparison in AeroCom phase I. *Atmos. Chem. Phys.* **2011**, *11*, 7781–7816. [CrossRef]
34. Benedetti, A.; Reid, J.S.; Knippertz, P.; Marsham, J.H.; Di Giuseppe, F.; Rémy, S.; Basart, S.; Boucher, O.; Brooks, I.M.; Menut, L.; et al. Status and future of numerical atmospheric aerosol prediction with a focus on data requirements. *Atmos. Chem. Phys.* **2018**, *18*, 10615–10643. [CrossRef]
35. Morcrette, J.-J.; Boucher, O.; Jones, L.; Salmond, D.; Bechtold, P.; Beljaars, A.; Benedetti, A.; Bonet, A.; Kaiser, J.W.; Razinger, M.; et al. Aerosol analysis and forecast in the European Centre for Medium-Range Weather Forecasts Integrated Forecast System: Forward modeling. *J. Geophys. Res. Atmos.* **2009**, *114*, D06206. [CrossRef]
36. Karagulian, F.; Temimi, M.; Ghebreyesus, D.; Weston, M.; Kondapalli, N.K.; Valappil, V.K.; Aldababesh, A.; Lyapustin, A.; Chaouch, N.; Al Hammadi, F.; et al. Analysis of a severe dust storm and its impact on air quality conditions using WRF-Chem modeling, satellite imagery, and ground observations. *Air Qual. Atmos. Health* **2019**, *12*, 453–470. [CrossRef]
37. Lee, E.-H.; Ha, J.-C.; Lee, S.-S.; Chun, Y. PM_{10} data assimilation over South Korea to Asian dust forecasting model with the optimal interpolation method. *Asia-Pac. J. Atmos. Sci.* **2013**, *49*, 73–85. [CrossRef]
38. Xu, C.; Zhang, H.; Luo, K.; Liu, J.; Shen, Y.; Qin, H.; Qu, Y.; Zhu, C.; Han, Z. A physics-guided machine learning framework for enhancing dust storm visibility prediction in arid and semi-arid regions. *Sci. Rep.* **2026**, *16*, 11824. [CrossRef] [PubMed]
39. Mei, S.; You, W.; Zhong, W.; Zang, Z.; Guo, J.; Cheng, X.; Gao, L. Improving aerosol forecasting through visibility data assimilation in WRF-Chem: Methodology and evaluation. *Atmos. Res.* **2026**, *327*, 108383. [CrossRef]
40. Shao, Y.; Raupach, M.R.; Findlater, P.A. Effect of saltation bombardment on the entrainment of dust by wind. *J. Geophys. Res. Atmos.* **1993**, *98*, 12719–12726. [CrossRef]
41. Shao, Y. Simplification of a dust emission scheme and comparison with data. *J. Geophys. Res. Atmos.* **2004**, *109*, D10202. [CrossRef]
42. Shao, Y. *Physics and Modelling of Wind Erosion*, 2nd ed.; Springer: Dordrecht, The Netherlands, 2008; Volume 37.
43. Shao, Y.; Lu, H. A simple expression for wind erosion threshold friction velocity. *J. Geophys. Res. Atmos.* **2000**, *105*, 22437–22443. [CrossRef]
44. Meng, Y.; Huang, N.; Dun, H.; Zhang, J.; Liu, R. A theoretical model of the influence of physical soil crusts on wind erosion under freeze–thaw action. *Catena* **2026**, *273*, 110406. [CrossRef]
45. Shao, Y.; Yang, Y.; Wang, J.; Song, Z.; Leslie, L.M.; Dong, C.; Zhang, Z.; Lin, Z.; Kanai, Y.; Yabuki, S.; et al. Northeast Asian dust storms: Real-time numerical prediction and validation. *J. Geophys. Res. Atmos.* **2003**, *108*, 4691. [CrossRef]
46. Chung, Y.; Kim, H.; Park, K.H.; Jhun, J.G.; Chen, S. Atmospheric loadings, concentrations and visibility associated with sandstorms: Satellite and meteorological analysis. *Water Air Soil Pollut. Focus* **2003**, *32*, 21–40. [CrossRef]
47. Dayan, U.; Ziv, B.; Shoob, T.; Enzel, Y. Suspended dust over southeastern mediterranean and its relation to atmospheric circulations. *Int. J. Climatol.* **2008**, *28*, 915–924. [CrossRef]